A Novel Strategy to Suppress Capacity and Voltage Fading of Li- and Mn-Rich Layered Oxide Cathode Material for Lithium-Ion Batteries

Shiming Zhang, Haitao Gu, Hongge Pan, Suhui Yang, Wubin Du, Xiang Li, Mingxia Gao, Yongfeng Liu,* Min Zhu, Liuzhang Ouyang, Dechao Jian, and Feng Pan*

Poor cycling stability is one of the key scientific issues needing to be solved for Li- and Mn-rich layered oxide cathode. In this paper, sodium carboxymethyl cellulose (CMC) is first used as a novel binder in $Li_{1.2}Ni_{0.13}Co_{0.13}Mn_{0.54}O_2$ cathode to enhance its cycling stability. Electrochemical performance is conducted by galvanostatic charge and discharge. Structure and morphology are characterized by X-ray diffraction, scanning electronic microscopy, high-resolution transmission electron microscopy, and X-ray photoelectron spectroscopy. Results reveal that the CMC as binder can not only stabilize the electrode structure by preventing the electrode materials to detach from the current collector but also suppress the voltage fading of the $Li_{1.2}Ni_{0.13}Co_{0.13}Mn_{0.54}O_2$ cathode due to Na^+ ions doping. Most importantly, the dissolution of metal elements from the cathode materials into the electrolyte is also inhibited.

1. Introduction

Lithium-ion batteries (LIBs) have been widely used as power sources of electric vehicles, 3C (computer, communication, and consumer electronic) products, and energy storage devices for renewable energy and smart grid.[1,2] However, the specific energy density of commercialized LIBs still cannot meet the requirements for practical applications. Success in these fields will mostly depend on further studying and developing new electrode materials with higher energy density.

Li- and Mn-rich layered oxide (LMRO) has been considered as a promising cathode material for the next-generation LIBs due to its high energy density more than 1000 W h kg^{-1}.[3–7] However, this material also suffers from several fatal drawbacks, such as severe capacity and voltage fading during cycling,[8–10] poor rate performance,[5,11,12] large initial irreversible capacity.[13,14] Among these problems, the capacity and voltage fading are the key scientific issues needing to be solved first. It is generally accepted that the structure instability of the LMRO cathode material is one of the intrinsic reasons of its fast capacity and voltage fading.[15–17] The phase transformation from layered to spinel structure gives rise to the crystal instability when the LMRO cathode is charged to 4.8 V.[18–21] The gradual growth of spinel phase during cycling brings about the appearance of a 3.0 V plateau resulting in the voltage fading and then consequently leading to the capacity fading.[22] On the other hand, the capacity fading is also caused by the dissolution of metal elements into the electrolyte.[23,24] Zheng et al.[8] believe that the loss of MnO and NiO results in the capacity loss of the $Li[Li_{0.2}Ni_{0.2}Mn_{0.6}]O_2$ electrode because of the formation of spinel phase and subsequent fragmentation and deactivation of transition metal ions. Moreover, the dissolution of metal elements is also due to the corrosion of hydroflouric acid (HF) coming from the reaction of the residual moisture with $LiPF_6$.[25]

Presently, several strategies have been proposed to suppress the capacity and voltage fading of LMRO cathode material. Surface coating with inert phases is one of the effective ways, such as MnO_x,[26,27] Al_2O_3,[28,29] MoO_3,[13] TiO_2,[30] ZrO_2,[31] $AlPO_4$,[32,33] AlF_3,[34,35] to stabilize the structure of the LMRO cathode materials. Choi et al.[36] reported that the $0.3Li_2MnO_3$-$0.7LiMn_{0.60}Ni_{0.25}Co_{0.15}O_2$ cathode material coated by Al_2O_3 improved not only its discharge capacity but also its cycling stability compared with the prinstine. Guo et al.[37] discovered that the $Li_{1.2}Ni_{0.16}Co_{0.068}$ $Mn_{0.56}O_2$ coated by 3 wt% MnO_2 delivered the capacity retention of 93% after 50 cycles. Chen et al.[38] demonstrated that $CePO_4$ layer coating onto

S. M. Zhang, Prof. H. G. Pan, S. H. Yang, W. B. Du, X. Li, Prof. M. X. Gao, Prof. Y. F. Liu
State Key Laboratory of Silicon Materials
Key Laboratory of Advanced Materials and Applications for Batteries of Zhejiang Province &
School of Materials Science and Engineering
Zhejiang University
Hangzhou 310027, P. R. China
E-mail: honggepan@zju.edu.cn; mselyf@zju.zju.edu.cn

H. Gu, D. Jian
Shanghai Institute of Space Power-Sources
Shanghai 201100, P. R. China

Prof. M. Zhu, Prof. L. Ouyang
School of Materials Science and Engineering
Key Laboratory of Advanced Energy Storage Materials of Guangdong Province
South China University of Technology
Guangzhou 510640, P. R. China

Prof. F. Pan
School of Advanced Materials
Peking University
Shenzhen Graduate School
Shenzhen 518055, P. R. China

DOI: 10.1002/aenm.201601066

$Li_{1.2}Ni_{0.13}Co_{0.13}Mn_{0.54}O_2$ could reduce the side reactions of the electrode with the electrolyte. Furthermore, ion doping also can significantly improve the cycling stability of the LMRO cathode material by stabilizing its crystal structure during cycling. Li et al.[39] found that K^+ ions doping in situ could stabilize the host crystal structure of the $Li_{1.2}Ni_{0.13}Co_{0.13}$ $Mn_{0.54}O_2$ cathode. The larger ionic radius of K^+ ions prohibited the formation of spinel structure during cycling.

However, these strategies emphasized solving the crystal structure instability of the LMRO cathode, and did not consider the stability problem of the electrode itself. In this work, based on the $Li_{1.2}Ni_{0.13}Co_{0.13}Mn_{0.54}O_2$ cathode, we try to find a new way to incoporate these two aspects to drastically enhance the electrochemical performance of the LMRO cathode material. Sodium carboxymethyl cellulose (CMC) possesses higher stickiness compared with that of traditional polyvinylidene fluoride (PVDF) binder, which can significantly stabilize the electrode structure. Most importantly, the Na^+ ions in CMC can perhaps dope into cathode material and exchange with Li^+ ions in LMRO during cycling, which consequently stabilize the crystal structure of the LMRO cathode materials.

2. Results and Discussion

2.1. Electrochemical Performance of the $Li_{1.2}Ni_{0.13}Co_{0.13}Mn_{0.54}O_2$ Cathode

In order to assess the electrochemical performance of the $Li_{1.2}Ni_{0.13}Co_{0.13}Mn_{0.54}O_2$ electrodes prepared with different binders, galvanostatic charge/discharge and cycling performance tests were conducted at different current density in the potential window of 2.0–4.8 V versus Li/Li^+ at 30 °C showing in Figure S1a and Table S1 (Supporting Information). The PAN10 and PVDF10 electrodes illustrate high electrochemical activity delivering initial discharge capacity of 306 and 297 mA h g^{-1}, and coulombic efficiency of 85% and 83% at 20 mA g^{-1}, respectively. By contrast, the CMC10 electrode shows the discharge capacity 247 mA h g^{-1} and coulombic efficiency of 80%, indicating that the $Li_{1.2}Ni_{0.13}Co_{0.13}Mn_{0.54}O_2$ cathode material with 10 wt% CMC as binder delivers poor electrochemical activity. However, for the CMC10 cathode, it is surprising to note that the discharge capacity increases to 269 mA h g^{-1} after 100 cycles at 20 mA g^{-1} with the capacity retention of 109% (**Figure 1**a; Table S1, Supporting Information), but the PAN10 and PVDF10 cathodes only demonstrate the capacity retention of 62% and 57%, respectively. For the prolonged cycling stability (Figure 1b), the CMC10 cathode exhibits the discharge capacity of 152 mA h g^{-1} and the capacity retention 83% of the initial discharge capacity of 183 mA h g^{-1} after 500 cycles at 200 mA g^{-1}, but the PAN10 and PVDF10 electrodes illustrate the poor prolonged cycling performance with capacity retention only 37% and 40%, respectively. It is very clear that the CMC as binder can reduce the electrochemical activity and coulombic efficiency of the $Li_{1.2}Ni_{0.13}Co_{0.13}Mn_{0.54}O_2$ electrode but significantly improve its cycling stability.

The electrochemical activity of the $Li_{1.2}Ni_{0.13}Co_{0.13}Mn_{0.54}O_2$ electrodes with PVDF10, PAN10, and CMC10 as binders were performed by an electrochemical impedance spectroscopy (EIS) technique. Nyquist plots of the PAN10, PVDF10, and

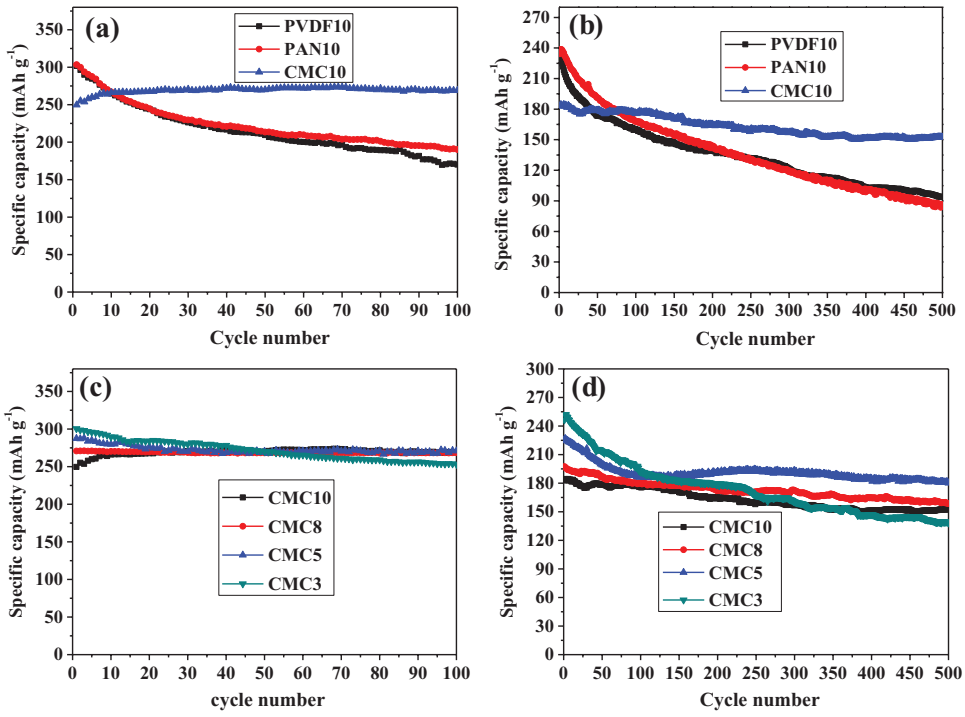

Figure 1. Cycling performance of the PVDF10, PAN10, and CMC10 electrodes at different current density in the potential window of 2.0 to 4.8 V versus Li/Li^+: a) 20 and b) 200 mA g^{-1}. Cycling performance of the CMC10, CMC8, CMC5, and CMC3 electrodes at different current density in the potential window of 2.0 to 4.8 V versus Li/Li^+: c) 20 and d) 200 mA g^{-1}.

CMC10 electrodes are compared in Figure S2a (Supporting Information). The equivalent circuit based on this Nyquist plots is applied to fit the primary data from EIS measurements (Figure S2c, Supporting Information).[40] The fitted results (Table S2, Supporting Information) demonstrate that the charge transfer resistance (R_{ct}) value (134.05 Ω) of the CMC10 electrode is larger than those of the PVDF10 and PAN10 (90.01 and 78.48 Ω) electrodes, which can be ascribed to the lower electronic conductivity of the CMC10 electrode.

In order to improve the electrochemical capacity of the $Li_{1.2}Ni_{0.13}Co_{0.13}Mn_{0.54}O_2$ cathode with the CMC as binder, we tried to decrease the content of the CMC to 8%, 5%, and 3% in the electrode, and their electrochemical performance is also represented in Figure S1b (Supporting Information). It can be seen that the CMC3, CMC5, CMC8, and CMC10 electrodes deliver the discharge specific capacity of 304, 285, 270, 247 mA h g^{-1} with the initial coulombic efficiency of 85%, 85%, 83%, and 80% at 20 mA g^{-1}, respectively. It is obvious that both the specific capacity and coulombic efficiency decrease with the increase of the CMC content. Figure S2b and Table S2 (Supporting Information) display the EIS results of the CMC3, CMC5, CMC8, and CMC10 electrodes. It can be found that the charge transfer resistance (R_{ct}) values of the electrode increase with the decrease of the CMC content, which suggests that reducing the CMC content can improve the electrochemical activity of the electrodes.

Figure 1c,d represents the cycling performance of the $Li_{1.2}Ni_{0.13}Co_{0.13}Mn_{0.54}O_2$ electrodes with different CMC content at 20 and 200 mA g^{-1}, and corresponding electrochemical data are also summarized in Table S1 (Supporting Information). It should be noted that the CMC3 electrode displays the highest initial discharge specific capacity but delivers the worst cycling stability with the capacity retention of only 75% after 100 cycles at 20 mA g^{-1} and 56% after 500 cycles at 200 mA g^{-1}, respectively. Although the CMC8 and CMC10 electrodes demonstrate the lower discharge specific capacity of 158 and 152 mA h g^{-1}, they deliver high capacity retention 83% and 80%, respectively. Therefore, we believe that the CMC5 electrode demonstrates the best overall electrochemical performance, exhibiting the high initial discharge capacity of 285 and 226 mA h g^{-1} with the capacity retention of 95% (246 mA h g^{-1}) after 50 cycles at 20 mA g^{-1} and 79% (180 mA h g^{-1}) after 500 cycles 200 mA g^{-1}, respectively.

Compared with the PVDF10 and PAN10 electrodes, the CMC5 electrode not only delivers high electrochemical activity, but also exhibits excellent prolonged cycling stability, presented in Figure S3a (Supporting Information). In addition, we also investigated the rate performance of the CMC5 electrode, displayed in Figure S3b (Supporting Information). It can be seen that this electrode delivers the rate specific capacity of 285, 266, 246, 226, 198, 177, and 156 mA h g^{-1} for the current density of 20, 40, 100, 200, 400, 1000, and 2000 mA h g^{-1}, respectively. Therefore, the $Li_{1.2}Ni_{0.13}Co_{0.13}Mn_{0.54}O_2$ electrode with the 5% CMC as binder holds both a prolonged cycling life and a superior high rate performance.

2.2. Mechanism Analysis for Suppressing Capacity and Voltage Fading of the $Li_{1.2}Ni_{0.13}Co_{0.13}Mn_{0.54}O_2$ Cathode

2.2.1. Stabilizing the Electrode Structure

First, the content of the polyacrylonitrile (PAN) binder in the electrodes was increased to 15%, 20%, and 25%, which was tried to enhance the cycling stability of the $Li_{1.2}Ni_{0.13}Co_{0.13}Mn_{0.54}O_2$ electrode. Contrary to our expectation, the results indicate that the cycling performance of these electrodes with the high content of PAN does not improve remarkably (Figure S4, Supporting Information), which means that the increase of the PAN content in the electrode cannot improve its cycling stability. Figure S5 (Supporting Information) shows the scanning electronic microscopy (SEM) images of the surface of the $Li_{1.2}Ni_{0.13}Co_{0.13}Mn_{0.54}O_2$ electrodes before cycling and after 500 cycles with different binders. It can be seen that the surfaces of all the electrodes integrate completely and show uniform distribution of the active materials, conductive agents, and binders. **Figure 2** shows the cross section SEM images after 500 cycles. It is surprising to find that the electrode materials

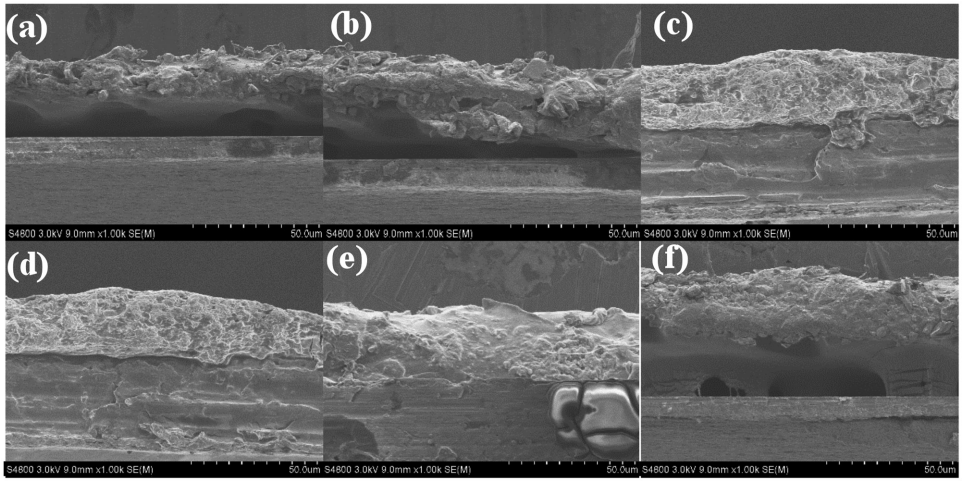

Figure 2. Cross section morphology images of different electrodes after 500 cycles at 200 mA g^{-1} in the potential window of 2.0–4.8 V versus Li/Li^+: a) PVDF10, b) PAN10, c) CMC10, d) CMC8, e) CMC5, and f) CMC3.

have detached completely from the Al current collector for the PAN10 and PVDF10 electrodes, but for the CMC5, CMC8, and CMC10 electrodes, they still keep integrated. This detachment of the PAN10 and PVDF10 electrodes is caused by their lower adhesive properties. The detachment of the electrode materials from the Al current collector severely affects their electric contact ability.

Figure 3 displays the EIS of the electrodes before cycling and after 500 cycles with different binders. The PVDF10, PAN10, and CMC3 electrodes show a larger charge transfer resistance (R_{ct}) after 500 cycles compared with that before cycling. By contrast, for the CMC5, CMC8, and CMC10 electrodes, the charge transfer resistances (R_{ct}) after 500 cycles almost remain unchanged compared with that before cycling. From these results, it can be concluded that the CMC as binder can significantly keep the integrity of the electrode during cycling and consequently markedly improve the cycling stability of the cathode.

In order to evaluate the adhesion of different binders, the interfacial properties between the Al current collector and the electrode materials, viscosity of the slurries, and peel test were performed. As shown in Figure S6a,b (Supporting Information), the electrode materials tightly adhere onto the Al collector for the CMC10 electrode, but for the PAN10 electrode, we can find an obvious boundary between the electrode materials and

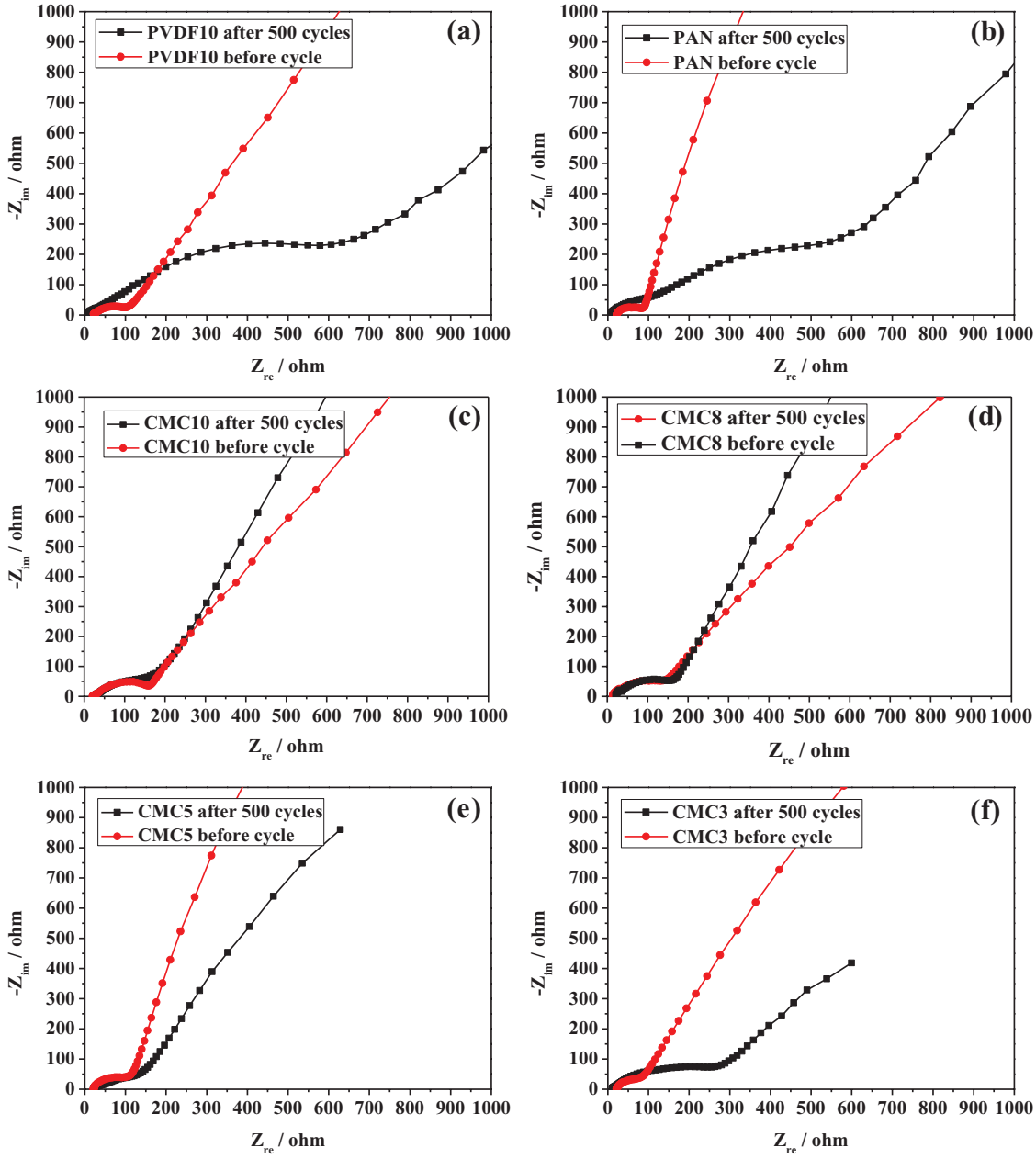

Figure 3. Nyquist plots of different electrodes before cycling and after 500 cycles at 200 mA g^{-1} from 0.01 HZ and 100000 HZ: a) PVDF10, b) PAN10, c) CMC10, d) CMC8, e) CMC5, and f) CMC3.

the Al current collector. Figure S6c (Supporting Information) shows that the viscosity of the CMC10 electrode slurry is about nine times higher than that of the PAN10 electrode slurry. In addition, the viscosity of the electrode slurry drastically increases with the increase of the content of the CMC binder. Moreover, the peel test (Figure S6d, Supporting Information) also clearly demonstrates that the electrode with the CMC as binder has excellent adhesive property than that with the PAN or PVDF as binder, and the adhesive strength also increases with the increase of the CMC content. The surface morphologies of the electrodes after the peel test are also shown and compared in Figure S7 (Supporting Information). For the PAN10 and PVDF10 electrodes, after the peel test, the electrode materials layer is totally peeled off from the Al current collector (Figure S7g,h, Supporting Information). However, a significant portion of electrode materials with CMC as binder still sticks to the Al current collector. These results indicate CMC as binder can significantly enhance adhesive property of the electrode.

2.2.2. Suppressing the Voltage Fading

Figure 4a displays the mid-point discharge voltage (MPV) fading curves of the PVDF10, PAN10, and CMC10 electrodes at different cycles at 20 mA g^{-1}. It can be seen that the MPV of the PVDF10 and PAN10 electrodes decreases fast from 3.55 to 2.78 V and from 3.57 to 2.85 V, respectively, with the MPV retention only 74% and 76% after 100 cycles. However, in the same conditions, the CMC10 electrode shows slowly MPV fading with the retention about 88% after 100 cycles from 3.52 to 3.10 V. The results indicate that the CMC as binder for the $Li_{1.2}Ni_{0.13}Co_{0.13}Mn_{0.54}O_2$ cathode can effectively suppress its voltage fading during cycling. From the discharge profiles of the electrodes at different cycles (Figure 4b–d), which reveals that the discharge plateaus of the PAN10 and PVDF10 electrodes decrease much faster than that of the CMC10 electrode. Furthermore, we can observe a long plateau below 3.0 V for the PAN10 and PVDF10 electrodes, but it has been remarkably suppressed for the CMC10 electrode.

In order to probe the phase transformation process of the $Li_{1.2}Ni_{0.13}Co_{0.13}Mn_{0.54}O_2$ cathode during cycling, the dQ/dV curves of the PVDF10, PAN10, and CMC10 electrodes at different cycles are studied (**Figure 5**), which are also used to investigate the relationship between the phase transformation and the voltage fading. The initial anodic peaks of all the electrodes at about 4.05 V can be attributed to the oxidation process of Ni^{2+} and Co^{3+} to higher oxidation states, and the anodic peaks at 4.55 V correspond to the electrochemical active process of $LiMnO_3$ like phase.[41] There are two cathodic peaks observed at about 3.76 and 3.35 V, respectively, which correspond to the reduction process of Ni^{4+} and Co^{4+} in the layered structure and Mn^{4+} in the spinel structure, respectively.[42] Moreover, it should be noted that the cathodic peak at 3.35 V does not appear for the CMC10 electrode in the initial discharge process, which indicates that there is no spinel phase transformation during the initial charge process for this electrode. After the second cycle, this cathodic peak gradually appears. Furthermore, it clearly shows that the cathodic peaks at 3.76 V of the PAN10 and

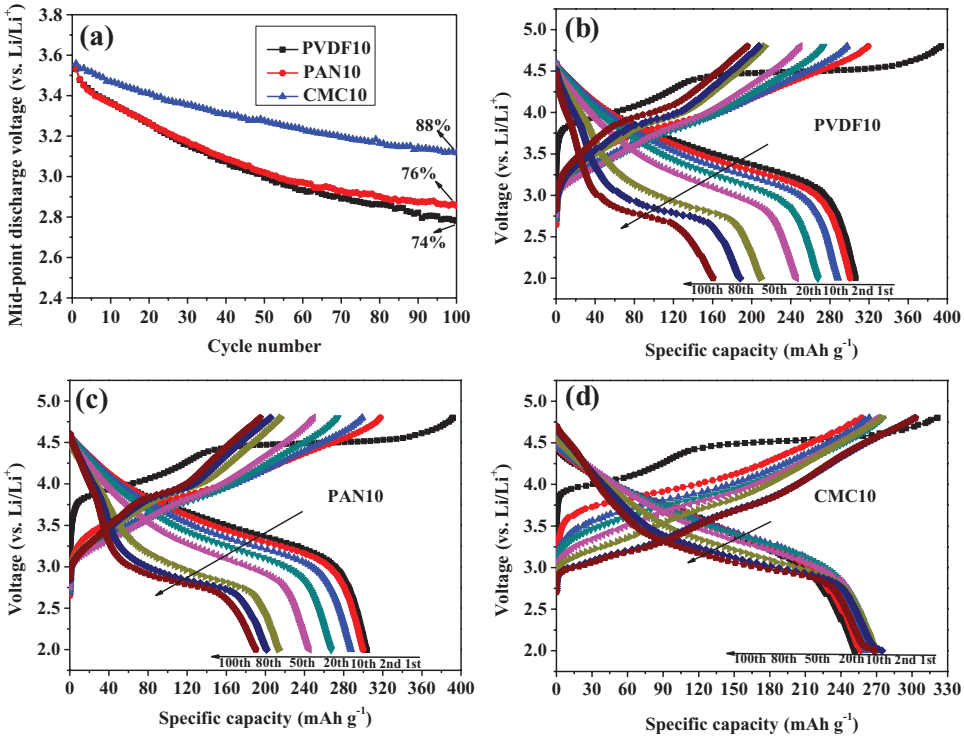

Figure 4. a) Mid-point discharge voltage fading curves of different electrodes during cycling at 20 mA g^{-1} in the potential window of 2.0–4.8 V versus Li/Li^+. Charge and discharge profiles of different electrodes at different cycles with different binders at 20 mA g^{-1} in the potential window of 2.0–4.8 V versus Li/Li^+: b)PVDF10, c) PAN10, and d) CMC10.

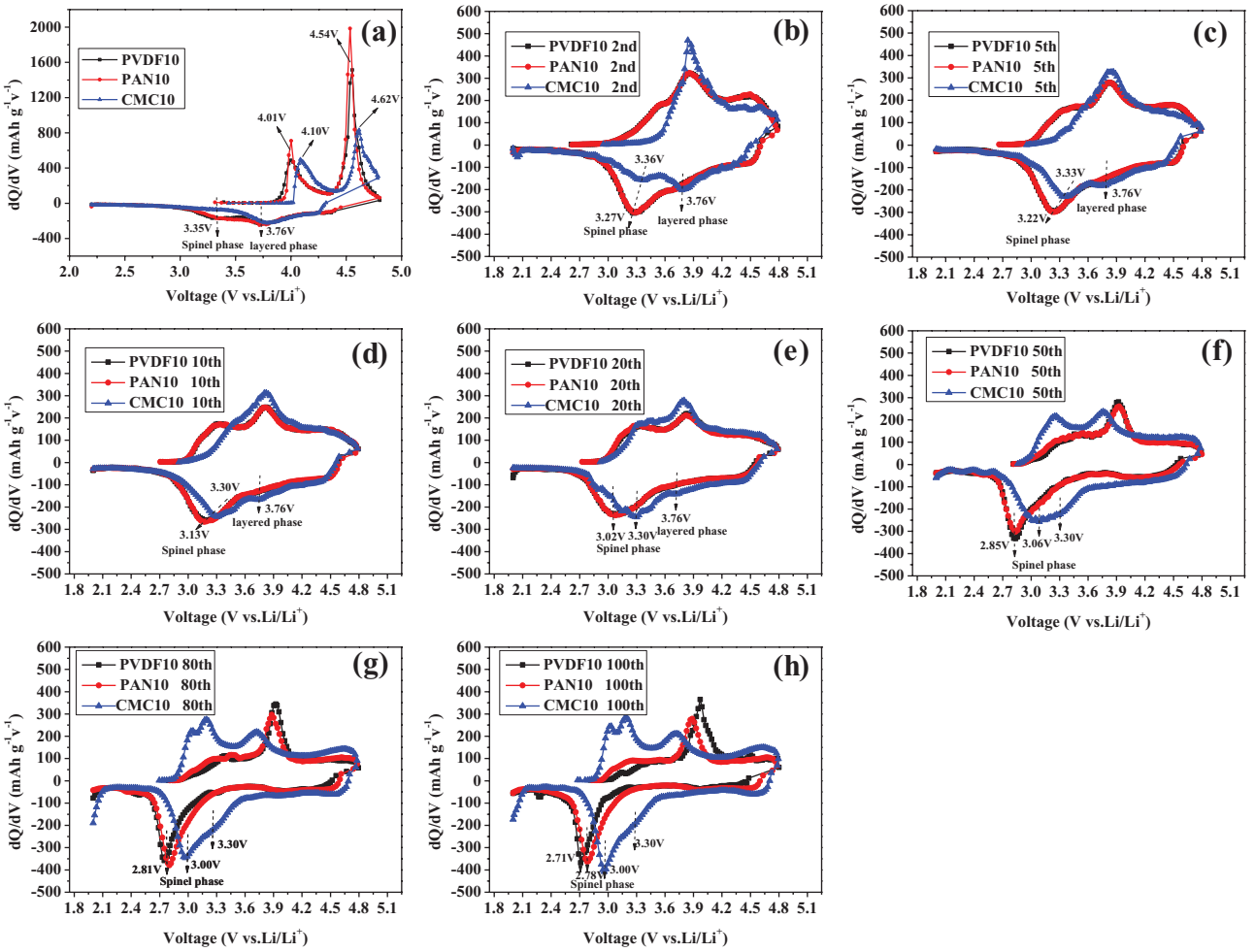

Figure 5. Comparisons of the differential capacity-versus-voltage (dQ/dV) curves of different electrodes at different cycles at 20 mA g^{-1} in the potential window of 2.0–4.8 V versus Li/Li^+: a)1st, b) 2nd, c)5th, d)10th, e)20th, f)50th, g)80th, and h)100th.

PVDF10 electrodes gradually disappear, but it is obviously suppressed for the CMC10 electrode. Most importantly, it is worthy noting that, for the PVDF10 and PAN10 electrodes, the other cathodic peaks below 3.35 V gradually shift to a lower potential from 3.35 to 2.71 V after 100 cycles, which can be attributed to the gradual formation of the spinel phase. In comparison, this cathodic peak of the CMC10 electrode only shifts to about 3.00 V after 100 cycles. As a conclusion, the CMC as binder can significantly suppress the transformation of the spinel phase for the $Li_{1.2}Ni_{0.13}Co_{0.13}Mn_{0.54}O_2$ cathode during cycling.

Figure 6 shows the X-ray diffraction (XRD) patterns and the corresponding refined data from XRD of the $Li_{1.2}Ni_{0.13}Co_{0.13}Mn_{0.54}O_2$ electrodes before cycling and after 500 cycles. As shown in Figure 6a, the XRD patterns of the PAN10, PVDF10, and CMC electrodes before cycling do not exhibit any obvious differences. All diffraction peaks can be indexed as a hexagonal unit cell with R-3m symmetry(ICSD #99890) as reported by Nahm and co-workers.[43] Figure 6b–e shows that all peaks shift to a lower angle after 500 cycles, but the peaks of the electrodes with the CMC as binder deliver much larger shift, and it increases with the rise of the CMC content. The variations in the cell parameters of the PAN10 and CMC electrodes before cycling and after 500 cycles were calculated by Rietveld refinement with General Structure Analysis System, and the refinement model is based on the $Li[Li_{1/5}Ni_{1/10}Co_{1/5}Mn_{1/2}]O_2$ with R-3m space group.[43] The obtained results are summarized in Table S3 (Supporting Information) and plotted in Figure 6f,g. The results illustrate the lattice parameters a and b remain almost constant, but the lattice parameter c and cell volume increase with the increase of the CMC content. Xie et al.[44] found the similar results in Na^+ doping $LiNi_{0.8}Co_{0.15}Al_{0.05}O_2$ cathode. They reveal that the peak of (003) reflections shifts toward a lower angle, indicating that the c-axis increases as the quantity of Na dopant grows, which is probably because Na^+ ions are thoroughly incorporated into the Li-ion layer, subsequently enlarging the Li layer spacing. Moreover, the percentage of Na^+ in the Li^+ site (I(003)/I(104)) increases with the increase of the CMC content, which demonstrates that a low degree of cation mixing is present in the electrodes with the CMC as binder. This phenomenon is also observed by Xie et al. in $Li_{1-x}Na_xNi_{0.8}Co_{0.15}Al_{0.05}O_2$ cathode materials.[44]

Figure S8 (Supporting Information) displays the XRD patterns of the $Li_{1.2}Ni_{0.13}Co_{0.13}Mn_{0.54}O_2$ cathode material at different cycles. It shows that the XRD peaks gradually shift to a

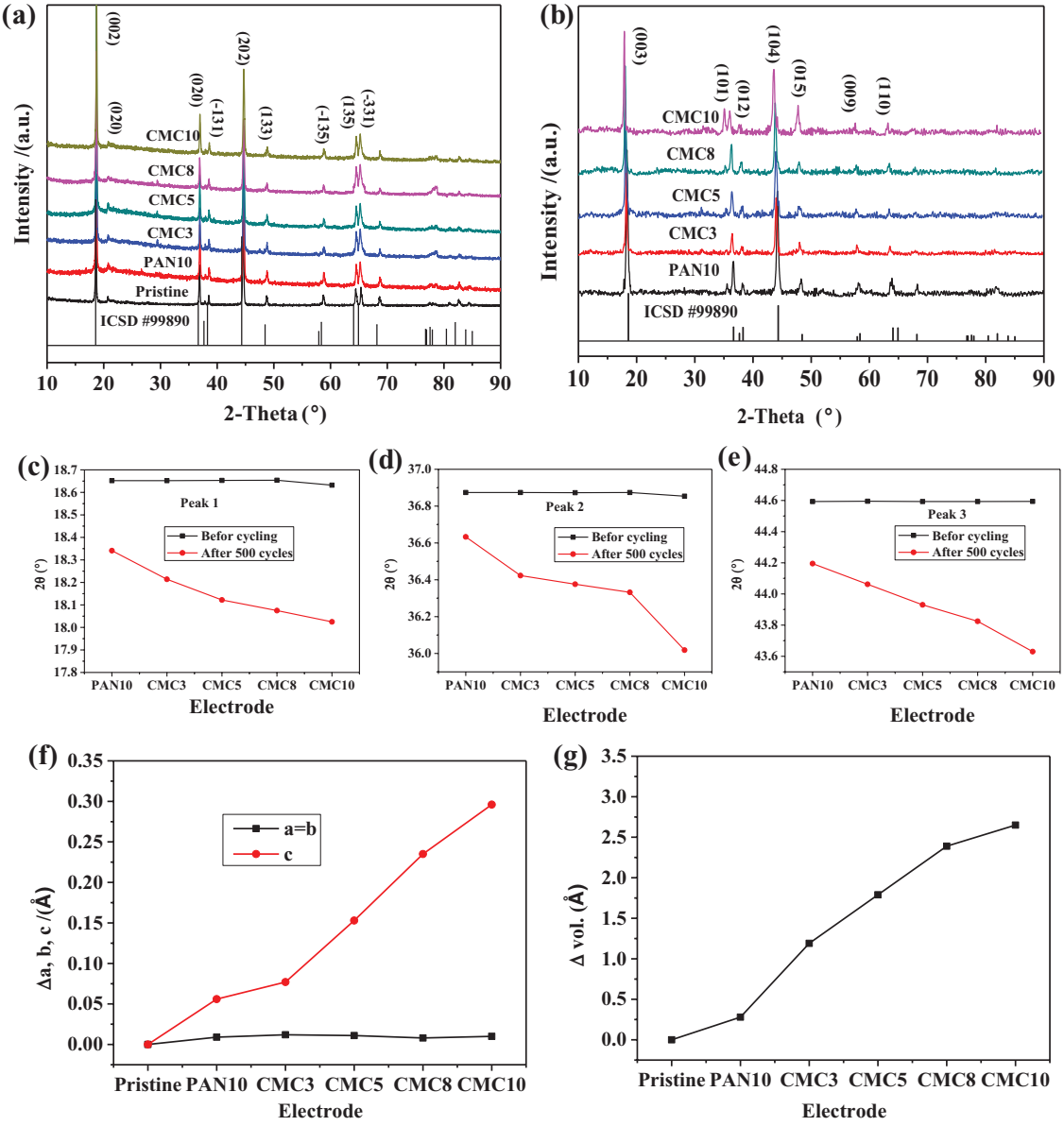

Figure 6. XRD patterns of different electrodes at different cycles: a) Before cycling, b) after 500 cycles at 200 mA g^{-1} in the potential window of 2.0–4.8 V versus Li/Li^+. The shift of 2θ of different electrodes at different cycles: c) Peak1 (18.57°), d) peak2 (36.66°), e) Peak3 (44.32°). The change of the cell parameters of different electrodes at different cycles: f) a/b/c, g) volume.

lower angle with the increase of the cycle number. In addition, the XRD peaks of the $Li_{1.2}Ni_{0.13}Co_{0.13}Mn_{0.54}O_2$ cathode material do not shift before cycling. It confirms that the Na^+ ions gradually enter into the lattice of the $Li_{1.2}Ni_{0.13}Co_{0.13}Mn_{0.54}O_2$ material during cycling instead of in the process of electrode preparation. The schematic diagram, as presented in **Figure 7**, can help us to understand the mechanism of Na^+ substituting Li^+ ions during cycling. Li^+ ions de-intercalate from the lithium layers forming extensive vacants, and then the de-intercalated Li^+ ions exchange with Na^+ ions provided by CMC. The Na^+ ions subsequently enter into the lithium layers at following discharge process.

The crucial step in the phase transformation from the layered to spinel structure is the migration of transition metal ions from transition metal layers to lithium layers, which is caused by the extensive vacant formation when Li^+ ions de-intercalate from the crystal after charging to high voltage over 4.8 V. Used the CMC as binder, the doped Na^+ ions do not migrate out from the crystal structure, which can significantly inhibit the migration of transition metal ions into Li^+ ion sites. Therefore, the phase transformation from layered to spinel structure is prevented, and consequently suppresses the capacity and voltage fading of the $Li_{1.2}Ni_{0.13}Co_{0.13}Mn_{0.54}O_2$ cathode material during cycling.

2.2.3. Inhibiting the Dissolution of Transition Metal Elements

The X-ray photoelectron spectroscopy (XPS) of these electrodes after 500 cycles was conducted to explore the dissolution of

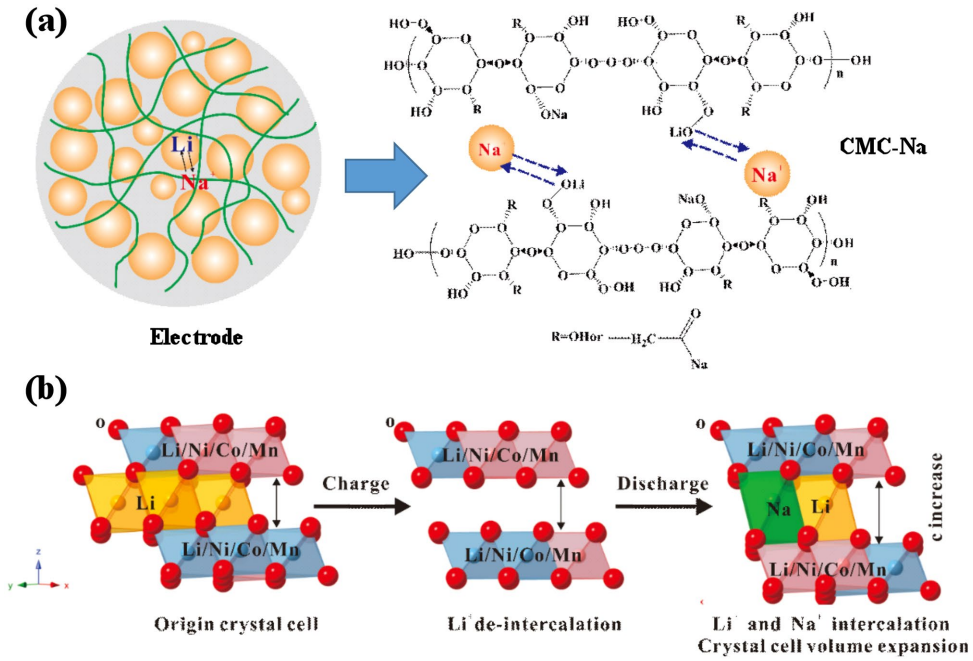

Figure 7. Schematic diagram of the ion-exchange of Li^+ with Na^+ provided by the CMC during cycling.

metal elements of the $Li_{1.2}Ni_{0.13}Co_{0.13}Mn_{0.54}O_2$ cathode material. In this experiment, Ar^+ ions were used to consecutively etch the electrodes from the surface to 50 and 100 nm, respectively. As illustrated in **Figure 8**, all spectra with respect to Ni 2p, Co 2p, and Mn 2p orbital have been compared in order to determine the variations in chemical state and content as a function of depth. Figure 8a–e shows the Ni 2p spectra of different electrodes. It can be seen that the Ni content on the surface of the PAN10, PVDF10, and CMC3 electrodes is much lower than that of 50 and 100 nm below the surface, but for the CMC10 and CMC5 electrodes, there is much more Ni on the surface. For the Co 2p spectra in Figure 8f–j, almost no Co elements are found on the surface for the PAN10, PVDF10, and CMC3 electrodes, but there are still lots of Co elements on the surface for the CMC10 and CMC5 electrodes. Similar to the Co 2p spectra, the spectra of Mn 2p (Figure 8k–o) demonstrate that there are almost no Mn elements on the surface for the PAN10, PVDF10, and CMC3 electrodes, but many Mn elements are still present on the surface for the CMC10 and CMC5 electrodes. Assuming the Ni, Co, and Mn dissolve into the electrolyte, we can find a large quantity of Li_2O phase residue on the surface of the electrodes. Figure S9 (Supporting Information) displays the XPS spectra of Li 1s and O1s of the electrodes after 500 cycles. It is very clear that there is much more Li_2O phase on the surface of the PAN10 electrode than that of the CMC5 electrode.

The dissolution of transition metal elements into the electrolyte is further confirmed by TEM (**Figure 9**). Figure 9a exhibits that the surface of as-prepared materials before cycling is smooth and integrated, but they become irregular and rough for the PAN10 (Figure 9b) and CMC5 (Figure 9c) electrodes after 500 cycles, which is caused by the dissolution of the Ni, Co, and Mn. It should be noted that this dissolution for the CMC5 electrode material is much slighter than that of the PAN10 electrode material. The HR-TEM lattice images (Figure 9d–f) and their corresponding fast Fourier transformation (FFT) (Figure 9j–l) show that the PAN10 electrode material cycled after 500 cycles demonstrates irregular lattice fringes with much lattice disorder, defects, and obvious polycrystalline rings, but the CMC5 electrode material exhibits relatively regular lattice fringes and well electronic diffraction spots. It is very clear, from the enlarged HR-TEM images (Figure 9g–i), that many more metal atoms have removed from the lattice for the PAN10 electrode cycled after 500 cycles compared with that of the CMC5 electrode. In addition, Figure S10 (Supporting Information) shows that the PVDF10 electrode also demonstrates similar results in comparison with that of the PAN10 electrode. These results suggest that a large quantity of Ni, Co, and Mn dissolve into the electrolyte for the PAN10 and PVDF10 electrodes, but this dissolution is suppressed for the electrodes with the CMC as binder.

In order to further confirm the dissolution of transition metal elements from the surface of the electrode materials, the EDS line scanning of the PAN10 and CMC5 electrode after 500 cycles were performed. Figure S11a,b (Supporting Information) shows that the PAN10 electrode materials suffer from severe surface corrosion than that of the CMC5 electrode materials after 500 cycles. The corresponding energy dispersive spectrometer (EDS) line scanning images are displayed in Figure S11c,d and Figure S11e,f (Supporting Information), respectively. The results clearly show that the electrode materials are corroded from the surface to the bulk, and the corrosion depth of the PAN10 electrode materials is about 47 nm, which is much larger than that of the CMC5 electrode materials (≈28 nm).

3. Conclusions

In summary, CMC as binder can significantly improve the cycling stability of the $Li_{1.2}Ni_{0.13}Co_{0.13}Mn_{0.54}O_2$ cathode. The

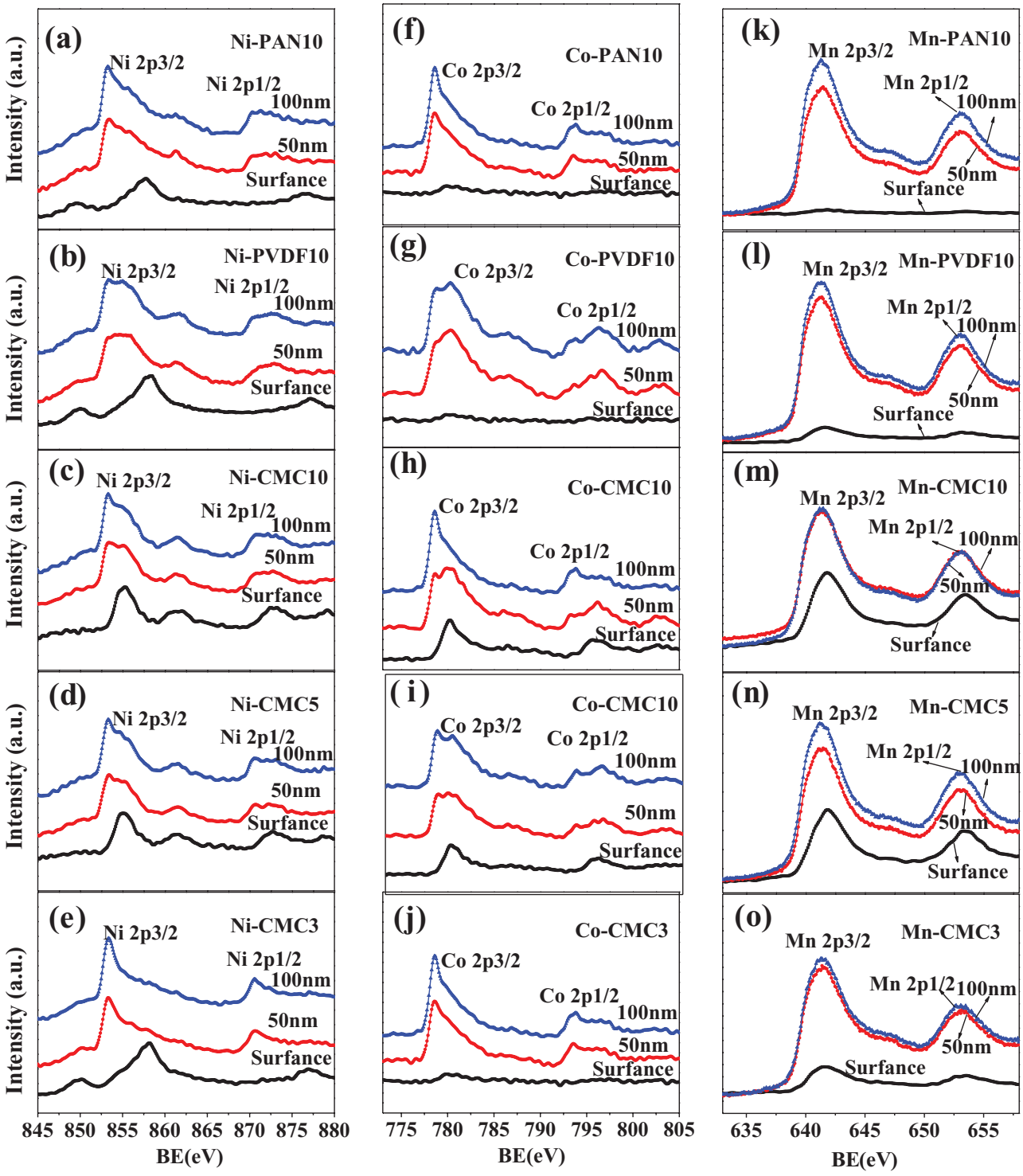

Figure 8. XPS spectra of the PAN10, PVDF10, CMC10, CMC5, and CMC3 electrodes after 500 cycles at 200 mA g^{-1} in the potential window of 2.0–4.8 V versus Li/Li^+, which were collected after the Ar^+ etching for 0, 50, 100 respectively: a–e) Ni 2p, f–j) Co2p, k–o) Mn 2p.

results indicate that the CMC5 electrode exhibits excellent overall electrochemical performance with the initial discharge capacity of 226 mA h g^{-1} and capacity retention of 79% after 500 cycles at 200 mA g^{-1}. Mechanisms using CMC as binder to improve the cycling stability of the $Li_{1.2}Ni_{0.13}Co_{0.13}Mn_{0.54}O_2$ cathode can be summarized as three following aspects: (1) stabilizing the electrode structure during cycling by preventing the electrode materials detaching from collector to ensure the electric contact ability; (2) suppressing the voltage fading by Na^+ ions doping. The XRD results confirm that the Na^+ ions

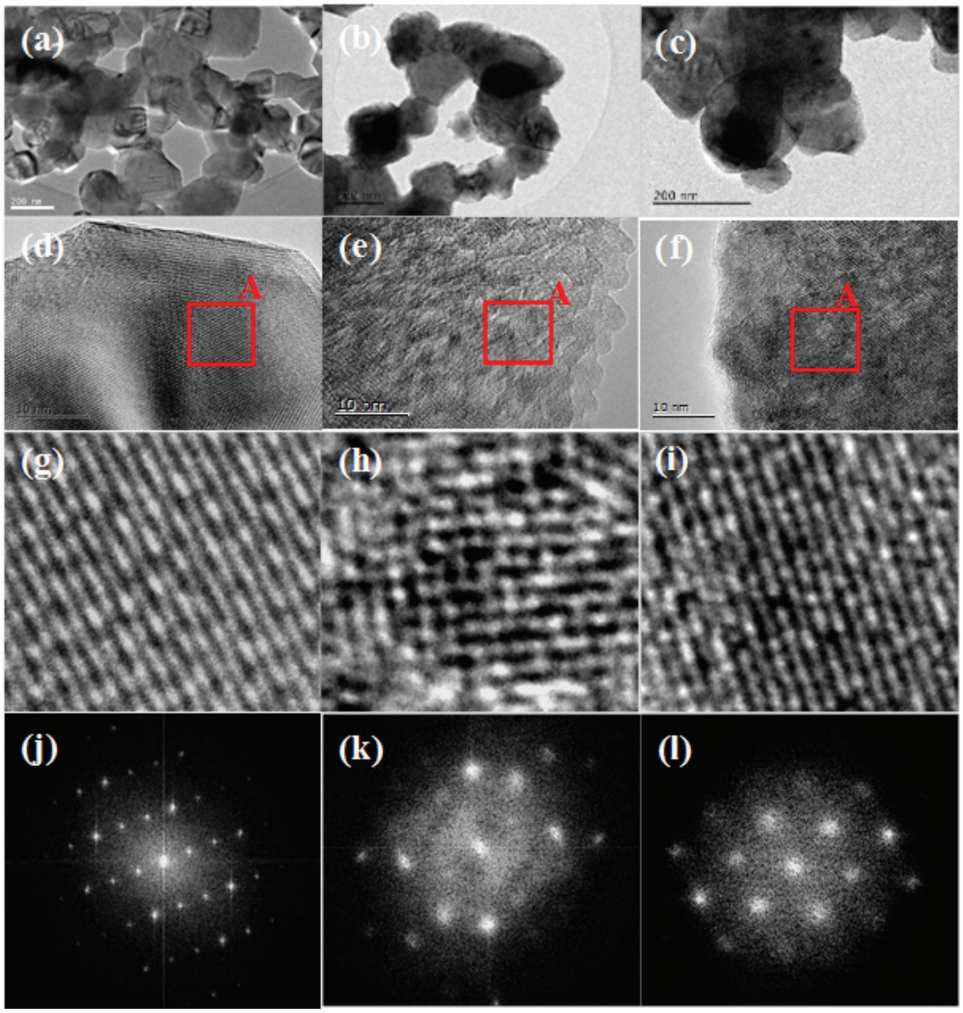

Figure 9. Low magnification TEM bright field images of the electrodes after 500 cycles at 200 mAg^{-1} in the potential window of 2.0–4.8 V versus Li/Li^+: a) Pristine $Li_{1.2}Ni_{0.13}Co_{0.13}Mn_{0.54}O_2$ powder, b) PAN10, and c) CMC5 electrode powders, respectively. The corresponding high-resolution transmission electron microscopy (HRTEM) images: d) Pristine $Li_{1.2}Ni_{0.13}Co_{0.13}Mn_{0.54}O_2$ powder, e) PAN10, and f) CMC5. The enlarged HRTEM images from the A regions of the (d–f): g) Pristine $Li_{1.2}Ni_{0.13}Co_{0.13}Mn_{0.54}O_2$ powder, h) PAN10, and i) CMC5. The FFT images of the HRTEM images from the (d–f): j) Pristine $Li_{1.2}Ni_{0.13}Co_{0.13}Mn_{0.54}O_2$ powder, k) PAN10, and l) CMC5.

can intercalate into the lattice by an ion-exchange way during discharge to stabilize the crystal structure. The charge and discharge and dQ/dV curves at different cycles demonstrate that phase transformation from the layered structure to spinel structure is suppressed due to the Na^+ ions doping and consequently inhibits the voltage fading; (3) the dissolution of metal elements of the $Li_{1.2}Ni_{0.13}Co_{0.13}Mn_{0.54}O_2$ electrodes with CMC as binder can be drastically inhibited during cycling.

4. Experimental Section

Synthesis of Samples: Precursor of the $Li_{1.2}Ni_{0.13}Co_{0.13}Mn_{0.54}O_2$ was synthesized by a spray pyrolysis method. Lithium acetate (LiAC, AR), manganese acetate (MnAC, AR), cobalt acetate (CoAC, AR), and nickel acetate (NiAC, AR) (a molar ratio of Li:Mn:Ni:Co = 1.2:0.54:0.13:0.13) were added to a 5000 mL deionized water with concentration of 0.3 mol L^{-1}, and then 0.8 mol citric acid was added to this solution as a complex reagent to inhibit the precipitation of metal salt. The mixed solution was then placed in a water bath kept at 80 °C stirring with an electric blender at 500 r min^{-1} for 1 h to form a spray solution, and then the spray solution was sent to the pulverizer with 200 °C high press gas by a peristaltic pump to obtain precursor powders. The collected precursor powders were then calcined at 900 °C for 10 h.

Preparation of Electrodes: First, the $Li_{1.2}Ni_{0.13}Co_{0.13}Mn_{0.54}O_2$ (1.6 g) and conductive agent super P(TIMCAL) (0.2 g) were added to a stainless steel ball mill jar (120 mL) with a weight ratio of 8:1, and then tungsten carbide (WC) balls (108 g) and ethanol (80 mL) were also added. Secondly, mixed materials were prepared via a high energy ball milling route with 400 r min^{-1} for 6 h. Finally, the obtained mixed materials were dried at 80 °C in an air-circulation oven for 12 h.

Composite electrode materials consist of different ratio active material ($Li_{1.2}Ni_{0.13}Co_{0.13}Mn_{0.54}O_2$), conductive agent (Super P), and binder (PVDF, PAN, or CMC) in different weight ratios. The slurries of the composite electrode materials were mixed with magnetic stirring for 4 h and then pasted onto aluminum foil to obtain electrodes. After that, prepared electrodes were dried at 120 °C in vacuum for 12 h to remove the solvent. The thickness of the electrodes is controlled near 30 µm for all samples. In order to distinguish different electrodes, they were

marked with different symbols according to different binders. Electrodes with the weight percentage of 10 wt% polyvinylidene fluoride (PVDF, CEA), and 10, 15, 20, and 25 wt% polyacrylonitrile (PAN, CEA) were denoted as PVDF10 and PAN10, PAN15, PAN20, PAN25, respectively. Electrodes with the weight percentage of 10, 8, 5, 3 wt% CMC (DS = 0.7, M_w = 90 000 Aldrich) were marked as CMC10, CMC8, CMC5, and CMC3, respectively.

Electrochemical Measurements: Electrochemical performance was characterized by 2025 coin-type cells. These cells were assembled in an Ar-filled glove box (water content <0.1 ppm) with lithium metal foil as negative and reference electrode and Celgard-2400 membrane as separator. The electrolyte consisted of a solution of 1 M $LiPF_6$ in ethylenecarbonate (EC), dimethycarbon, and diethycarbonate (DEC) with a volume ratio of 1:1:1. The galvanostatic charge and discharge tests were performed on a multichannel battery testing system (NEWARE BST-610, China) at different current with a voltage window of 2.0–4.8 V versus Li^+/Li at 30 °C. The EIS was carried out by a VMP system (Biologic, English]) with an AC amplitude of 5 mV in the frequency range from 0.01 to 100000 Hz at 30 °C.

Characterization: Crystal structures of the $Li_{1.2}Ni_{0.13}Co_{0.13}Mn_{0.54}O_2$ powders and electrode materials were investigated by XRD measurements (X'Pert PRO, PANalytical) using Kα radiation at 2θ ranging from 20° to 90° at a scan rate of 2° min^{-1}. Scanning electronic microscopy (FE-SEM, S-4800, Hitachi) and high resolution transmission electron microscopy (HR-TEM) (TEM, Techai G2 F30, FEI Company) were used to investigate the morphology, particle size, and micro-crystal structure. XPS measurements were performed using an X-ray photoelectron spectrometer (ESCALAB 250Xi, Thermo Scientific) equipped with an Al Kα X-ray radiation source (photon energy 1486.6 eV) for the electrode powders after 500 cycles. The thickness of the XPS Ar^+ sputtered layer was determined by etching time with sputtered rate of 5 nm min^{-1}. In this test, the etching rate was 5 nm min^{-1}.The tested $Li_{1.2}Ni_{0.13}Co_{0.13}Mn_{0.54}O_2$ electrode materials were cycled for different cycles at the current density of 200 mA g^{-1}, and then disassembled in Ar-filled glove box (water content <0.1 ppm). The disassembled electrodes were rinsed with DEC to remove excess electrolyte from the electrodes and then dried at room temperature in Ar-filled glove box for 24 h. The composite powders were collected by being separated from the aluminum current collectors.

Viscosity and Peel Tests: The viscosity of slurries was analyzed by using a rotational rheometer (AR1000, TA Instruments Ltd., UK). The peel strength was measured with a micro material tester (Instron 5848, Instron Company, USA). A 15 mm wide and 30 mm long anode sample was attached to a 3 M adhesive tape. The adhesive tape was removed by peeling at the angle of 90° with a constant displacement rate of 50 mm min^{-1}. The applied load was continuously measured, and force/time plots were produced.

Supporting Information

Supporting Information is available from the Wiley Online Library or from the author.

Acknowledgements

This work was supported by the National Natural Science Foundation of PR China (Grant No. 51571178), Natural Science Foundation of Zhejiang Province (Grant No. LY14E010004), Program for University Innovative Research Team of the Ministry of Education of China (Grant No. IRT13037), the Fundamental Research Funds for the Central Universities (Grant No. 2014XZZX005) (Grant No. 2014XZZX005), Aerospace Science and Technology Innovation Fund of CASC, Innovative Research Groups of the National Natural Science Foundation of China (Grant No. NSFC51621001), and National Materials Genome Project (Grant No. 2016YFB0700600).

Received: May 21, 2016
Revised: July 3, 2016
Published online:

[1] A. M. Gaikwad, B. V. Khau, G. Davies, B. Hertzberg, D. A. Steingart, A. C. Arias, *Adv. Energy Mater.* **2015**, *5*, 1401389.
[2] M. S. Whittingham, *Chem. Rev.* **2014**, *114*, 11413.
[3] H. Yu, H. Zhou, J. Phys. *Chem. Lett.* **2013**, *4*, 1268.
[4] N. Yabuuchi, R. Hara, M. Kajiyama, K. Kubota, T. Ishigaki, A. Hoshikawa, S. Komaba, *Adv. Energy Mater.* **2014**, *4*, 1301453.
[5] X. Q. Yu, Y. C. Lyu, L. Gu, H. M. Wu, S. M. Bak, Y. N. Zhou, K. Amine, S. N. Ehrlich, H. Li, K. W. Nam, X. Q. Yang, *Adv. Energy Mater.* **2014**, *4*, 1300950.
[6] J. S. Kim, C. S. Johnson, J. T. Vaughey, M. M. Thackeray, S. A. Hackney, *Chem. Mater.* **2004**, *16*, 1996.
[7] K. Numata, C. Sakaki, S. Yamanaka, *Solid State Ion.* **1999**, *117*, 257.
[8] J. M. Zheng, M. Gu, J. Xiao, P. J. Zuo, C. M. Wang, J. G. Zhang, *Nano Lett.* **2013**, *13*, 3824.
[9] Y. Li, J. Bareno, M. Bettge, D. P. Abraham, *J. Electrochem. Soc.* **2015**, *162*, A155.
[10] X. K. Yang, D. Wang, R. Z. Yu, Y. S. Bai, H. B. Shu, L. Ge, H. P. Guo, Q. L. Wei, L. Liu, X. Y. Wang, *J. Mater. Chem. A* **2014**, *2*, 3899.
[11] M. N. Ates, S. Mukerjee, K. M. Abraham, *J. Electrochem. Soc.* **2014**, *161*, A355.
[12] B. Song, H. Liu, Z. Liu, P. Xiao, M. O. Lai, L. Lu, *Sci. Rep.* **2013**, *3*, 3094.
[13] F. Wu, Z. Wang, Y. F. Su, N. Yan, L. Y. Bao, S. Chen, *J. Power Sources* **2014**, *247*, 20.
[14] C. S. Johnson, J. S. Kim, C. Lefief, N. Li, J. T. Vaughey, M. M. Thackeray, *Electrochem. Commun.* **2004**, *6*, 1085.
[15] M. N. Ates, Q. Y. Jia, A. Shah, A. Busnaina, S. Mukerjee, K. M. Abraham, *J. Electrochem. Soc.* **2014**, *161*, A290.
[16] J. R. Croy, D. Kim, M. Balasubramanian, K. Gallagher, S. H. Kang, M. M. Thackeray, *J. Electrochem. Soc.* **2012**, *159*, A781.
[17] S. H. Yu, T. Yoon, J. Mun, S. Park, Y. S. Kang, J. H. Park, S. M. Oh, Y. E. Sung, *J. Mater. Chem. A* **2013**, *1*, 2833.
[18] Y. K. Sun, *Electrochem. Commun.* **2001**, *3*, 199.
[19] S. Tan, Z. R. Zhang, Y. X. Li, Y. Li, J. M. Zheng, Z. B. Zhou, Y. Yang, *J. Electrochem. Soc.* **2013**, *160*, A285.
[20] D. Mohanty, A. Huq, E. A. Payzant, A. S. Sefat, J. Li, D. P. Abraham, D. L. Wood, C. Daniel, *Chem. Mater.* **2013**, *25*, 4064.
[21] K. A. Jarvis, C. C. Wang, A. Manthiram, P. J. Ferreira, *J. Mater. Chem. A* **2014**, *2*, 1353.
[22] Y. Wu, C. Ma, J. H. Yang, Z. C. Li, L. F. Allard, C. D. Liang, M. F. Chi, *J. Mater. Chem. A* **2015**, *3*, 5385.
[23] J. Shim, R. Kostecki, T. Richardson, X. Song, K. A. Striebel, *J. Power Sources* **2002**, *112*, 222.
[24] L. Yang, M. Takahashi, B. Wang, *Electrochim. Acta* **2006**, *51*, 3228.
[25] J. G. Han, S. J. Lee, J. Lee, J. S. Kim, K. T. Lee, N. S. Choi, *ACS Appl. Mater. Inter.* **2015**, *7*, 8319.
[26] A. Kumar, R. Nazzario, L. Torres-Castro, A. Pena-Duarte, M. S. Tomar, *Int. J. Hydrogen Energy* **2015**, *40*, 4931.
[27] S. J. Shi, J. P. Tu, Y. Y. Tang, X. Y. Liu, Y. Q. Zhang, X. L. Wang, C. D. Gu, *Electrochim. Acta* **2013**, *88*, 671.
[28] Y. Q. Wu, J. Ming, L. H. Zhuo, Y. C. Yu, F. Y. Zhao, *Electrochim. Acta* **2013**, *113*, 54.
[29] Y. J. Kang, J. H. Kim, S. W. Lee, Y. K. Sun, *Electrochim. Acta* **2005**, *50*, 4784.
[30] J. M. Zheng, J. Li, Z. R. Zhang, X. J. Guo, Y. Yang, *Solid State Ion.* **2008**, *179*, 1794.
[31] R. J. Gummow, N. Sharma, R. S. Feng, G. H. Han, Y. H. He, *J. Electrochem. Soc.* **2013**, *160*, A1856.

[32] Y. Wu, A. V. Murugan, A. Manthiram, *J. Electrochem. Soc.* **2008**, *155*, A635.
[33] K. J. Rosina, M. Jiang, D. L. Zeng, E. Salager, A. S. Best, C. P. Grey, *J. Mater. Chem.* **2012**, *22*, 20602.
[34] J. M. Zheng, Z. R. Zhang, X. B. Wu, Z. X. Dong, Z. Zhu, Y. Yang, *J. Electrochem. Soc.* **2008**, *155*, A775.
[35] F. Amalraj, M. Talianker, B. Markovsky, L. Burlaka, N. Leifer, G. Goobes, E. M. Erickson, O. Haik, J. Grinblat, E. Zinigrad, D. Aurbach, J. K. Lampert, J. Y. Shin, M. Schulz-Dobrick, A. Garsuch, *J. Electrochem. Soc.* **2013**, *160*, A2220.
[36] M. Choi, G. Ham, B. S. Jin, S. M. Lee, Y. M. Lee, G. X. Wang, H. S. Kim, *J. Alloys Compd.* **2014**, *608*, 110.
[37] S. H. Guo, H. J. Yu, P. Liu, X. Z. Liu, D. Li, M. W. Chen, M. Ishida, H. S. Zhou, *J. Mater. Chem. A* **2014**, *2*, 4422.
[38] J. J. Chen, Z. D. Li, H. F. Xiang, W. W. Wu, S. Cheng, L. J. Zhang, Q. S. Wang, Y. C. Wu, *RSC Adv.* **2015**, *5*, 3031.
[39] Q. Li, G. S. Li, C. C. Fu, D. Luo, J. M. Fan, L. P. Li, *ACS Appl. Mater. Interfaces* **2014**, *6*, 10330.
[40] J. W. Kou, L. Chen, Y. F. Su, L. Y. Bao, J. Wang, N. Li, W. K. Li, M. Wang, S. Chen, F. Wu, *ACS Appl. Mater. Interfaces* **2015**, *7*, 17910.
[41] N. Yabuuchi, K. Yoshii, S. T. Myung, I. Nakai, S. Komaba, *J. Am. Chem. Soc.* **2011**, *133*, 4404.
[42] Z. X. Yu, S. L. Shang, M. L. Gordin, A. Mousharraf, Z. K. Liu, D. H. Wang, *J. Mater. Chem. A* **2015**, *3*, 17376.
[43] K. S. Park, M. H. Cho, S. J. Jin, K. S. Nahm, Y. S. Hong, *Solid State Ion.* **2004**, *171*, 141.
[44] H. Xie, K. Du, G. Hu, Z. Peng, Y. Cao, *J. Phys. Chem. C* **2016**, *120*, 3235.